

Supplementary Information

Prediction of Solid Oxide Fuel Cell Cathode Activity with First-Principles Descriptors

Yueh-Lin Lee¹, Jesper Kleis², Jan Rossmeisl², Yang Shao-Horn³, and Dane Morgan^{1}*

¹ Department of Materials Science and Engineering, University of Wisconsin–Madison,
Madison, Wisconsin 53706,

² *Center for Atomic-scale Materials Design (CAMD), Department of Physics, Technical
University of Denmark, DK-2800, Lyngby, Denmark*

³ *Department of Mechanical Engineering and Department of Materials Science and
Engineering, Massachusetts Institute of Technology, 77 Massachusetts Ave., Cambridge,
Massachusetts 02139*

E-mail: ddmorgan@wisc.edu

Table of Content for the Supplementary Information

Index	Page
Introduction	2
Section 1	3-4
Section 2	5-6
Section 3	7-11
Section 4	12-14
Section 5	15-17
Section 6	18-22
Section 7	23-26
Section 8	27-28
References	29-32
Table S1	4
Table S2	17
Table S3	19
Figure S1	10-11
Figure S2	13-14
Figure S3	21
Figure S4	22
Figure S5	25
Figure S6	26
Figure S7	28

Introduction:

The Supplementary Information (SI) is divided into eight sections. Section 1 summarizes the corresponding references of the collected experimental area specific resistance (ASR) and surface exchange coefficient (k^*) data shown in Figure 1 and Figure 2 of the main paper. Section 2 describes the calculation approach. Section 3 describes the effects of the choice of U_{eff} parameter and the magnetic ordering on the energetics. Section 4 discusses the correlations between the surface O p -band center vs. oxygen reduction reaction (ORR) relevant energies and compares the surface and bulk O p -band center correlations. Section 5 compares our O p -band descriptor to the widely used d -band center descriptor. Section 6 considers how oxygen nonstoichiometry could impact the O p -band position and our descriptor accuracy. Section 7 considers the use of the bulk vacancy formation energy in-place of the O p -band as a descriptor. Finally, Section 8 discusses issues of perovskite stability and our descriptor approach.

Section 1: References for the Collected Experimental ASR and k^* Data in the Main Paper

Table S1 summarizes the references of the collected experimental ASR¹⁻²⁰ and k^* ^{7, 11, 21-28} data shown in Figure 1 and Figure 2 of the main paper.

Table S1. Summary of the references for the experimental area specific resistances (ASR) and surface exchange coefficients (k^*) of perovskite type transition metal oxides at $T \approx 1000$ K and $P(O_2) = 0.2 \sim 1$ bar shown in Figure 1 and Figure 2 in the main paper. Also included are the electrolytes used in experiments and compositions used in the simulations to approximate the true experimental compositions.

System	Simulated Composition	References of Exp. ASR	References of Exp. k^*
$Ba_{0.5}Sr_{0.5}Co_{0.8}Fe_{0.2}O_{3-\delta}$ (BSCF)	$Ba_{0.5}Sr_{0.5}Co_{0.75}Fe_{0.25}O_3$	0.01 $\Omega \cdot cm^2$, Ref. ¹ (T=973K) on SDC* 0.035 $\Omega \cdot cm^2$, Ref. ² (T=973K) on GDC* 0.018 $\Omega \cdot cm^2$, Ref. ³ (T=973K) on GDC*	Ref. ²¹ (T=973K)
$Sm_{0.5}Sr_{0.5}CoO_{3-\delta}$ (SSC)	$Sm_{0.5}Sr_{0.5}CoO_3$	0.10 $\Omega \cdot cm^2$, Ref. ⁴ (T=973K) on SDC* 0.07 $\Omega \cdot cm^2$, Ref. ⁵ (T=973K) on LSGM* 0.08 $\Omega \cdot cm^2$, Ref. ⁶ (Extrapolation to T=1000K) on SDC*	Ref. ²² (T=973K)
$Pr_{0.5}Ba_{0.5}CoO_{3-\delta}$ (PBCO)	$Pr_{0.5}Ba_{0.5}CoO_3$	0.1 $\Omega \cdot cm^2$, Ref. ⁷ (Extrapolation to T=1000K) on GDC* 0.3 $\Omega \cdot cm^2$, Ref. ⁸ (Extrapolation to T=1000K) on SDC* 0.08 $\Omega \cdot cm^2$, Ref. ⁹ (T=973K) on SDC*	Ref. ⁷ (extrapolation to T=1000K)
$Gd_{0.5}Ba_{0.5}CoO_{3-\delta}$ (GBCO)	$Gd_{0.5}Ba_{0.5}CoO_3$	0.3 $\Omega \cdot cm^2$, Ref. ¹⁰ (Extrapolation to T=1000K) on GDC* 0.1 $\Omega \cdot cm^2$, Ref. ¹¹ (Extrapolation to T=1000K) on GDC* 0.15 $\Omega \cdot cm^2$, Ref. ¹² (T=1023K) on SDC*	Ref. ¹¹ (T=959K) Ref. ²³ (extrapolation to T=1000K)
$La_{0.6}Sr_{0.4}Co_{0.2}Fe_{0.8}O_{3-\delta}$ (LSCF)	$La_{0.625}Sr_{0.375}Co_{0.25}Fe_{0.75}O_3$	0.33 $\Omega \cdot cm^2$, Ref. ¹³ (T=973K) on SDC* over YSZ 0.22 $\Omega \cdot cm^2$, Ref. ¹⁴ (T=973K) on GDC* 0.24 $\Omega \cdot cm^2$, Ref. ¹⁵ (T=999K) on GDC*	Ref. ²⁴ (T=1000K) Ref. ²⁵ (T=1073K)
$La_{0.8}Sr_{0.2}CoO_{3-\delta}$ (LSC)	$La_{0.75}Sr_{0.25}CoO_3$	0.41 $\Omega \cdot cm^2$, Ref. ¹⁴ (T=973K) on GDC* 2.19 $\Omega \cdot cm^2$, Ref. ¹⁶ (T=973K) on LSGM* 0.58 $\Omega \cdot cm^2$, Ref. ¹⁷ (T=973K) on GDC* 0.24 $\Omega \cdot cm^2$, Ref. ¹⁷ (T=973K) on SDC/SSZ*	Ref. ²⁶ (T=973K)
$LaCoO_{3-\delta}$ (LCO)	$LaCoO_3$	3.24 $\Omega \cdot cm^2$, Ref. ¹⁸ (T=973K) on YSZ*	Ref. ²⁷ (T=973K)
$La_{0.8}Sr_{0.2}MnO_{3-\delta}$ ^{14,19} $La_{0.85}Sr_{0.15}MnO_{3-\delta}$ ²⁰ (LSM)	$La_{0.75}Sr_{0.25}MnO_3$	405.5 $\Omega \cdot cm^2$, Ref. ¹⁴ (T=973K) on YSZ* 38.1 $\Omega \cdot cm^2$, Ref. ²⁰ (T=973K) on YSZ* 2.67 $\Omega \cdot cm^2$, Ref. ¹⁹ (T=973K) on GDC* 7.82 $\Omega \cdot cm^2$, Ref. ¹⁹ (T=973K) on YSZ*	Ref. ²⁶ (T=973K)
$LaMnO_{3-\delta}$ (LMO)	$LaMnO_3$	433.5 $\Omega \cdot cm^2$, Ref. ²⁰ (T=973K) on YSZ*	Ref. ²⁸ (T=973K)

*SDC: Sm doped ceria; GDC: Gd doped ceria; LSGM: $La_{0.8}Sr_{0.2}Ga_{0.8}Mg_{0.2}O_{3-\delta}$; YSZ: Y doped zirconia; SSZ: Sc and Ce doped zirconia.

Section 2: Simulation Approach for Surfaces and the Disordered Bulk Phases

The energetics of surface reactions are calculated using asymmetric 8-layer (001) surface slabs in periodic boundary conditions with 10 Å vacuum between the two surfaces. The bottom 2 layers of the slab are fixed to the bulk coordinates, while the remaining atoms are internally relaxed in the supercell. The reaction energetics will change if fewer layers are used, however we have found that the correlations of energies with *O-p* band center are conserved when the reaction energetics (surface vacancy formation/oxygen adsorption) are calculated with just 4-layers. Thus, for the trend discussion we find it sufficient to perform the time-consuming calculations of the kinetic barriers such as O₂ splitting, O_{ad} hopping, and surface O vacancy migration using a 4-layer slab.

In some materials (specifically, Ba_{0.5}Sr_{0.5}Co_{0.75}Fe_{0.25}O₃, Sm_{0.5}Sr_{0.5}CoO₃, and La_{0.625}Sr_{0.375}Co_{0.25}Fe_{0.75}O₃) there are high-concentrations of disordered mixtures of multiple cations on one or more sublattices. In addition, if off-stoichiometry is included through the presence of oxygen vacancies (see Section 5), there is further disorder on the oxygen sublattice. These disordered structures do not have uniquely specified atomic configurations in a small unit cell first-principles calculation. These systems are therefore modeled with the Special Quasi-random Structures (SQS) approach²⁹, where the cations are arranged within a finite unit cell (here a 2×2×2 perovskite cell) to be as random as possible in terms of local correlations. Specifically, for the cation and anion sublattice disordered phases *O p*-band center results based on 10 (La_{0.625}Sr_{0.375}Co_{0.25}Fe_{0.75}O₃), 12 (Sm_{0.5}Sr_{0.5}CoO_{2.875}), and 24 (Ba_{0.5}Sr_{0.5}Co_{0.75}Fe_{0.25}O_{2.5}) SQS's within the 2×2×2 perovskite supercell are used. The same number of SQS are used for both the

stoichiometric and non-stoichiometric (anion vacancy) cases, although the structures are different. Note that SQS's were not used in disordered solid solution phases with more dilute alloying concentrations, e.g., $\text{La}_{0.75}\text{Sr}_{0.25}\text{MnO}_3$. This approximate treatment is possible because at more dilute concentrations there are either few or just one configuration accessible in our relatively small unit cells, and when there are multiple configurations the configurational dependence of calculated values is typically quite low. An effective O *p*-band center is determined by the weighted average of the SQS O *p*-band centers, where the weighting is given by the Boltzmann factor for the energy of the SQS evaluated at 1000 K. The range of the O *p*-band centers of the quasi-random structures is generally represented with a horizontal bar in our figures, with the ends of the bar corresponding to the extremes of the SQS results. The results for these partially ordered SQS studies on stoichiometric systems are shown in Figures 1 and 2 in the main text, and on non-stoichiometric systems (*i.e.*, with oxygen vacancies based on experimental values) in Figures S2 and S3 in this SI. The most stable SQS were also used to find the vacancy formation energies used in Figures S4 and S5.

Section 3: Effects of the U_{eff} Parameter and Magnetic Ordering on the Reaction Energies

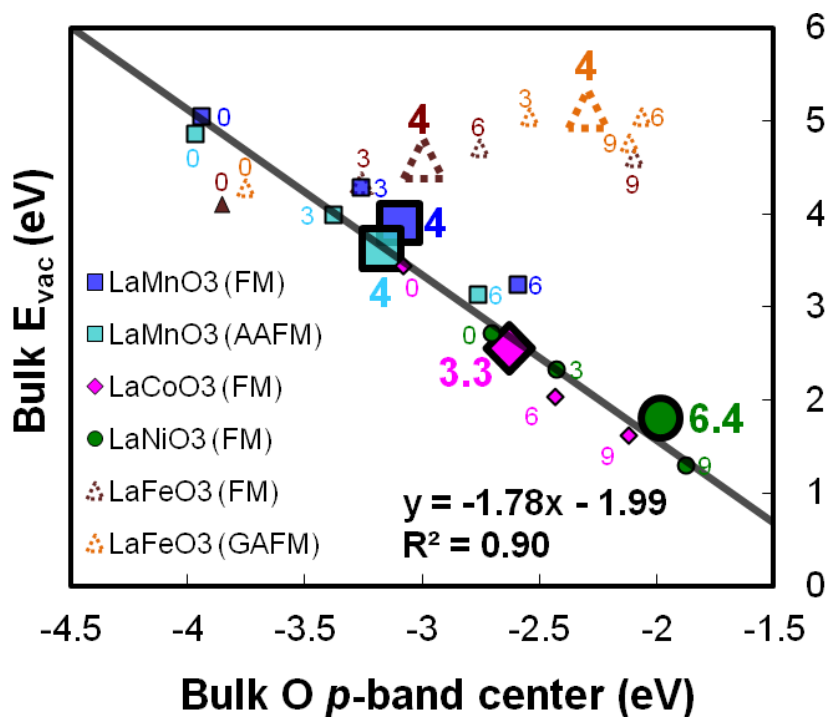
Due to the dependence on the implementation of the DFT+ U approach and the variation of the effective Hubbard U (U_{eff}) between bulk and surface, the optimal choice of U_{eff} is hard to estimate for surface reactions. It is therefore important to determine if key correlations identified in this work depend strongly on the choice of U_{eff} . We have evaluated the O p -band center (relative to the Fermi level) and bulk oxygen vacancy formation energy (E_{vac}), (001) BO₂ surface E_{vac} , and (001) BO₂ surface oxygen binding energy (E_{O-B}) for our LaBO₃ (B = Mn, Fe, Co, Ni) systems for a wide range of U_{eff} s (0~9 eV, as shown in Figure S1). We find these key energies for the ORR all scale linearly with the bulk O p -band center except for insulating LaFeO₃ at higher U_{eff} s, where the materials has a significant band gap. It is noted that the experimental ground state A-type antiferromagnetic (AFM) LaMnO₃ is also an insulator with a reported band gap of 1~2 eV³⁰⁻³², while both our calculated FM and A-type AFM LaMnO₃ are metallic. This metallic state occurs because the cubic supercell used to simulate the high temperature structures in our calculations suppresses Jahn-Teller distortion and results in no gaps for LaMnO₃ from $U_{eff} = 0\sim 6$ eV (see Ref. ³³ for more detailed discussions). The overall results suggest the selection of an optimal U_{eff} for the system will mainly cause a shift of the reaction energies along the linear correlations (deviations at 0.1 eV scale may arise from spin states and relaxation) when the material is metallic. The data for the insulating LaFeO₃ systems clearly deviate from the linear trend established by the electron-conducting perovskites. This suggests that the linear correlations between the ORR energetics and the O p -band center descriptor are valid for electron-conducting

perovskites but not for semiconducting or insulating oxide systems, where the existence of band gaps causes additional energy penalty that does not correlate with the O p -band center descriptor in the reaction energetics. Such distinction also corresponds to the observation that the collective empirical correlation of oxygen surface exchange k^* vs. tracer diffusion coefficient D^* among various perovskite oxides shows separation of groups for good and poor electronic conductors³⁴⁻³⁵. Furthermore, this result implies that different mechanisms should be operative for electron-rich and electron poor materials³⁶. The extension of our work to find a more general descriptor which includes insulating oxides is underway.

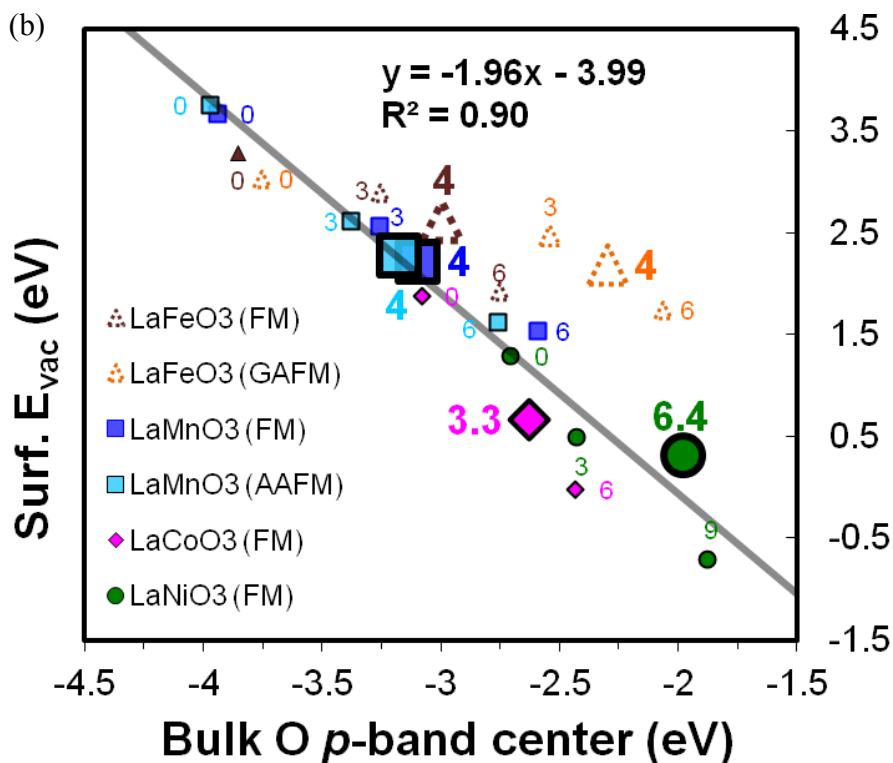
At solid oxide fuel cell temperatures (~ 800 - 1300 K), LaMnO_3 , LaFeO_3 , LaCoO_3 and LaNiO_3 all become paramagnetic. While the true paramagnetic phase is difficult to simulate in DFT calculations, in Figure S1 we compare reaction energetics using both ground state AFM (A-type AFM (AAFM) for LaMnO_3 and G-type AFM (GAFM) for LaFeO_3) and ferromagnetic (FM) states to investigate the influence of magnetic states on the linear correlation of the reaction energetics vs. O p -band center. It is found that for the Jahn-Teller distortion suppressed (with no band gap) FM and AAFM LaMnO_3 (square symbols in Figure S1), there is only slight shift in the reaction energetics vs. the O p -band centers at the same U_{eff} and all the data remain close to the linear correlation. On the other hand, the FM and GAFM LaFeO_3 (triangle symbols in Figure S1) both deviate from the linear correlation, and the energetics vs. the O p -band center data exhibits significant shift at the same U_{eff} . This suggests that the influence of magnetic states on the reaction energetics vs. the O p -band center for metallic systems is small, but could become significant for insulating systems (lead to significant change in the O p -

band centers). Generally, for transition metal oxides, the AFM states tend to give larger band gaps than the FM states, and FM states exhibits a more conducting character than AFM states. Since good electronic conductivity is essential for SOFC cathode materials and the use of AFM states for the perovskites could deviate from the electron-rich nature under typical SOFC operating conditions, we therefore use the FM state to approximate the metallic characteristics.

(a)



(b)



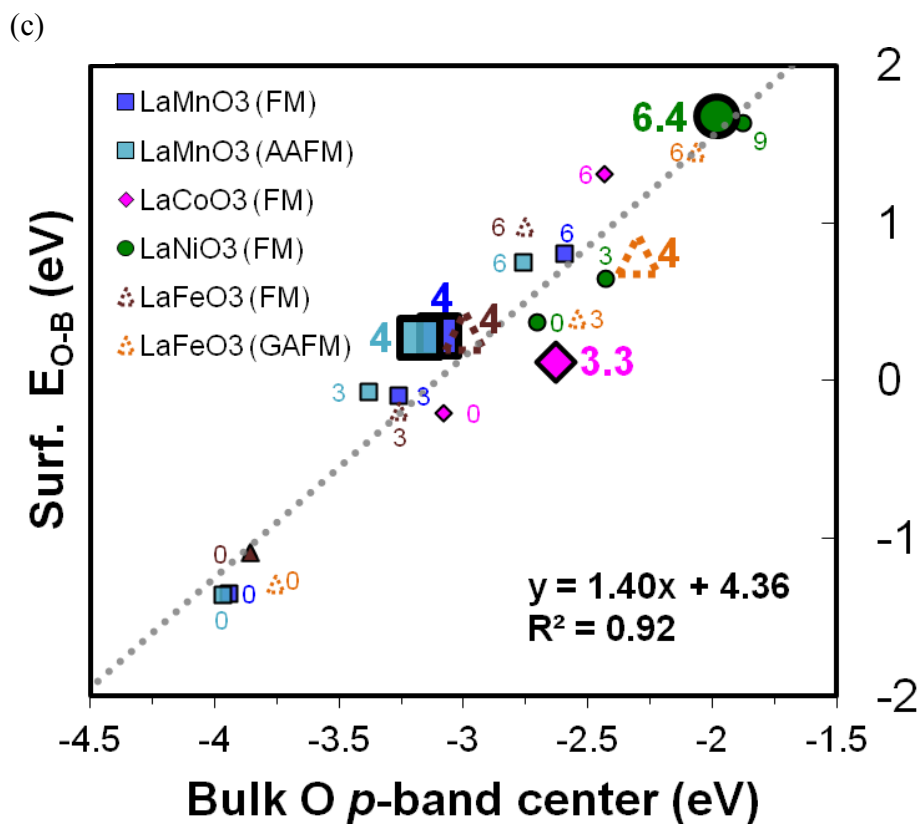


Figure S1: The LaBO₃ bulk oxygen vacancy (a), BO₂ surface oxygen vacancy (b), and BO₂ surface O above B site adsorption energies (c) as a function of the bulk O *p*-band center, where the bulk O *p*-band center is calculated from the projected density of states (DOS) of all the oxygen in the perfect bulk. Each point corresponds to different B metal cations at different U_{eff} values (U_{eff} is labeled next to the data points), and the enlarged points represent the results at the optimal U_{eff} from Ref. ³⁷. The fitted lines are only for solid symbol data (metallic systems with no band gap), and the empty symbols represent the insulating systems with band gaps.

Section 4: Surface O *p*-band center vs. the ORR relevant energies

Figure S2 shows the LaBO₃ (001) BO₂ surface oxygen vacancy (part a) and BO₂ surface O above B site adsorption energies (part b) as a function of the surface O *p*-band center. The surface O *p*-band center is calculated from the projected DOS of oxygen in the top two surface layers of a perfect stoichiometric slab (these include a BO₂ and LaO layer). The results show that the surface O *p*-band center also correlates well with both the surface oxygen vacancy formation and oxygen binding at B-site energies. Good correlations of surface O-*p* band center with other calculated ORR relevant energies are also shown in Table S2. These results suggest the surface O *p*-band, along with the bulk O *p*-band, could also be an effective ORR activity descriptor. Nonetheless, by comparing Figure S1 and Figure S2 (or results in Table S2, we see that the use of surface O *p*-band center does not improve on the correlations with the ORR relevant energies as compared to the bulk O *p*-band center results. This result supports the use the bulk O-*p* band center as the ORR activity descriptor as it is easier to determine than the surface O *p*-band center.

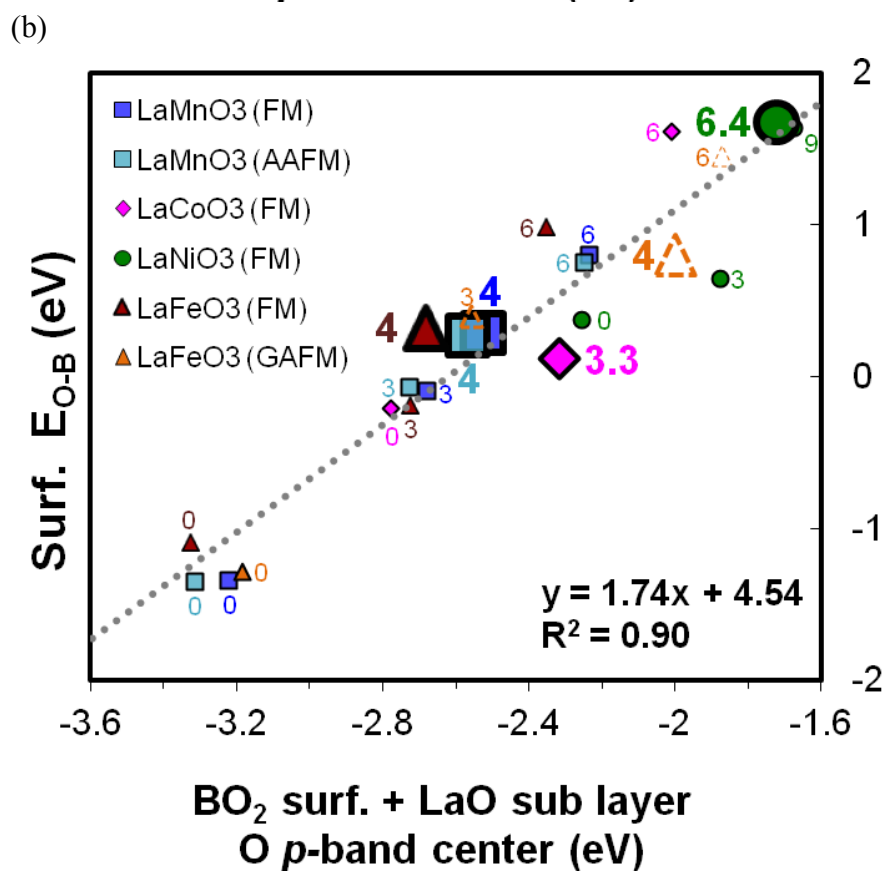
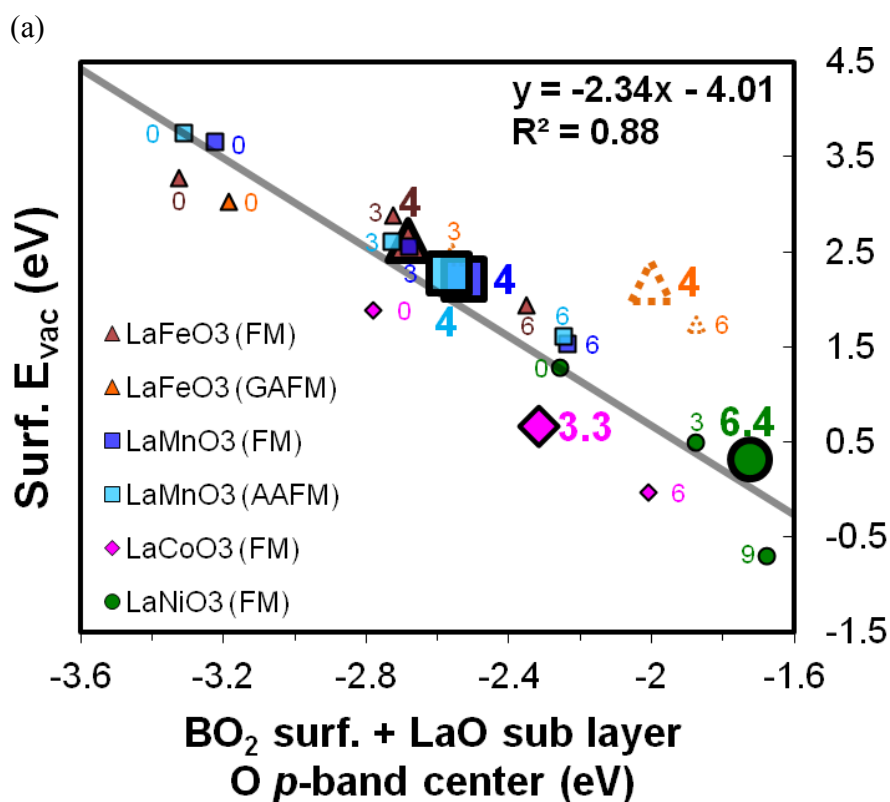


Figure S2: The LaBO_3 (001) BO_2 surface oxygen vacancy (a), and BO_2 surface O above B site adsorption energies (b) as a function of the surface O p -band center. The surface O p -band center is calculated from the projected DOS of oxygen in the top two surface layers of a perfect stoichiometric slab. Each point corresponds to different B metal cations at different U_{eff} values (U_{eff} is labeled next to the data points), and the enlarged points represent the results at the optimal U_{eff} from Ref. ³⁷. The fitted lines are only for solid symbol data (metallic systems with no band gap), and the empty symbols represent the insulating systems with band gaps. Notice that the surface effect accompanied with electron/hole doping (e.g. reduction on the LaO surface and oxidation on the BO_2 surfaces) can alter the electronic structure, so an insulating bulk with a band gap could have metallic BO_2 surfaces. This surface metallization occurs for FM LaFeO_3 at $U_{\text{eff}} = 3, 4$ and 6 eV and G-type AFM LaFeO_3 at $U_{\text{eff}} = 3$ eV.

Section 5. Correlations of ORR Reaction Energies with the O *p*-Band Center vs. the *d*-Band Center

Table S2 summarizes the correlations of all our calculated LaBO₃ (B=Mn, Fe, Co, and Ni) ORR relevant energetics vs. the O *p*-band and transition metal *d*-band centers of both bulk and surfaces, including surface oxygen binding, hopping, bulk and surface vacancy formation, and O₂ dissociation energies. Generally, both the bulk and surface O *p*-band centers correlate remarkably well with the interaction energetics, with mean value errors from the linear relations on the scale of 100 meV. At first sight, the O_{bridge} interaction does not correlate with the O *p*-band center ($R^2 \sim 0.50$). However, unavoidable DFT errors are more pronounced for calculations at sites that are weakly interacting (as O_{bridge}). Thus these sites show worse linear correlations (smaller R^2 values) than the stronger interacting sites (e.g. O at B,...). The R^2 values for the *d*-band center correlations are significantly lower than for the O *p*-band center, suggesting the *d*-band center is a poor descriptor for the ORR energy data.

Interestingly, slopes of oxidation reactions (e.g. surface oxygen adsorption) are positive, while those of reduction reactions (e.g. oxygen vacancy formation) are negative, consistent with electrons moving from and to the O *p*-band, respectively. Furthermore, the slopes of the linear correlations for reaction energetics are close to the theoretical amount of charge transfer in the reactions, and the slopes of kinetic barriers vs. the O *p*-band centers may correspond to the amount of charge transferred to the saddle point intermediates. For example, the slopes of the O binding at B-site (surface oxygen vacancy formation energy) vs. O *p*-band center are 1.40 (-1.96) for the bulk and 1.74 (-2.34) for the surface, close to the value of 2 expected for transferring 2 electrons to the

bound oxygen (releasing 2 electron by forming a surface oxygen vacancy). No such physical correlation seems to exist for the slopes of the fits to the *d*-band center.

Overall, the summarized results in Table S2 suggest the calculated ORR reaction energetics are better described by the calculated O *p*-band center than the *d*-band center for the electron-rich perovskite systems.

Table S2. A summary table of the linear correlations between ORR proxy energies and the calculated LaBO₃ bulk and surface *O p*-band center (bold fonts) and the *d* band center (in parentheses). Ideal electron transfer coefficients listed in the last column are based on number of electrons transferred in the reaction equations. Results for the bulk simulation values are in bold.

Property	R ²		Mean absolute error (eV)		Slope (per O)		Ideal electron transfer per O
	<i>O p</i> -band center (<i>d</i> band center)		<i>O p</i> -band center (<i>d</i> band center)		<i>O p</i> -band center (<i>d</i> band center)		
	Bulk	Surf.	Bulk	Surf.	Bulk	Surf.	
BO ₂ Surface O Binding at B	0.92 (0.38)	0.90 (0.50)	0.23 (0.58)	0.24 (0.48)	1.40 (-0.63)	1.74 (-0.75)	2
BO ₂ Surface O ₂ Binding at B	0.74 (0.44)	0.76 (0.60)	0.06 (0.08)	0.07 (0.07)	0.20 (-0.11)	0.25 (-0.13)	~0.5 ^a
BO ₂ Surface O Binding at Bridge	0.51 (0.07)	0.51 (0.11)	0.12 (0.21)	0.12 (0.20)	-0.32 (0.08)	-0.39 (0.11)	0 ^b
LaO Surface O adsorption	0.91 (0.40)	0.91 (0.23)	0.29 (0.81)	0.32 (0.90)	2.02 (-0.80)	2.33 (-0.69)	2
Vacancy Bulk	0.90 (0.48)	--	0.27 (0.67)	--	-1.78 (0.86)	--	-2
Vacancy Surface	0.90 (0.25)	0.88 (0.33)	0.25 (0.87)	0.36 (0.81)	-1.96 (0.72)	-2.34 (0.84)	-2
O B-B hop	0.65 (0.19)	0.62 (0.30)	0.17 (0.18)	0.15 (0.19)	-0.40 (0.15)	-0.72 (0.19)	--
O ₂ Split	0.90 (0.20)	0.77 (0.43)	0.15 (0.41)	0.23 (0.36)	0.90 (-0.43)	1.33 (-0.43)	~1 ^c
O ₂ Split (w/vacancy)	0.53 (0.43)	0.60 (0.33)	0.21 (0.27)	0.24 (0.29)	0.43 (-0.20)	0.62 (-0.28)	~1 ^d

^a superoxide like species

^b peroxide like species (an adsorbed O bonded to surface layer O and tilted toward surface B)

^c transition state between the O₂ binding at B and splitted O binding at B on the BO₂ surface

^d transition state between the O binding at Bridge and the O binding at B on the BO₂ surface

Section 6: Oxygen Nonstoichiometry and Descriptor Accuracy

For the O *p*-band center vs. ASR and k^* relations shown in Figure 1 and Figure 2 of the main text, we have used the bulk O *p*-band center calculated for the stoichiometric, undefected bulk material. However, under typical SOFC conditions many of the SOFC materials will have large concentrations of point defects and be off-stoichiometric. It is important to demonstrate that when more realistic stoichiometries are used in the calculations that the O *p*-band center is still a good descriptor for the area specific resistance (ASR) and the oxygen surface exchange coefficient (k^*).

In order to incorporate experimental oxygen nonstoichiometry information³⁸⁻⁴⁶ anion or cation vacancies are created in the simulated perovskite supercells to yield compositions close to those obtained under SOFC conditions (we chose the ambient air condition at $T=1000$ K in this work). The specific compositions from experiment and those used in the calculations are given in detail in Table S3. We generally used $2\times 2\times 2$ perovskite supercells as in Ref.³³ in the simulations except a $2\times 2\times 4$ perovskite supercell is used for overstoichiometric $\text{LaMnO}_{3+\delta}$, where one A-site and one B-site cation vacancy are created with the largest possible separation in the $2\times 2\times 4$ supercell to reduce their repulsive defect interaction. Due to the use of finite size supercells the smallest change in composition possible for the cation doping concentration and oxygen nonstoichiometry in our simulations are $1/8$ and $1/24$, respectively ($1/16$ and $1/48$ for the $2\times 2\times 4$ supercell). For $\text{PrBaCo}_2\text{O}_{5+\delta}$ and $\text{GdBaCo}_2\text{O}_{5+\delta}$, the A-site ordered double perovskite phase²³ is used in the calculations.

Table S3. Experimental nonstoichiometry of perovskite type transition metal oxides at $T \approx 1000$ K and $P(\text{O}_2) \approx 0.2$ atm and corresponding simulated compositions.

System	Simulated Composition	Exp. δ
$\text{Ba}_{0.5}\text{Sr}_{0.5}\text{Co}_{0.8}\text{Fe}_{0.2}\text{O}_{3-\delta}$ (BSCF)	$\text{Ba}_{0.5}\text{Sr}_{0.5}\text{Co}_{0.75}\text{Fe}_{0.25}\text{O}_{2.5}$	0.26~0.68 ($T=973$ K, $P(\text{O}_2)=0.1$ atm) ³⁸⁻⁴⁰
$\text{Sm}_{0.5}\text{Sr}_{0.5}\text{CoO}_{3-\delta}$ (SSC)	$\text{Sm}_{0.5}\text{Sr}_{0.5}\text{CoO}_{2.875}$	Assume δ close to that of $\text{La}_{0.5}\text{Sr}_{0.5}\text{CoO}_{3-\delta}$ at $T=1000$ K and $P(\text{O}_2)=0.2$ atm ⁴¹
$\text{Pr}_{0.5}\text{Ba}_{0.5}\text{CoO}_{3-\delta}$ (PBCO)	$\text{Pr}_{0.5}\text{Ba}_{0.5}\text{CoO}_{2.75}$	0.27 ($T=1073$ K, $P(\text{O}_2)=0.2$ atm) ⁴²
$\text{Gd}_{0.5}\text{Ba}_{0.5}\text{CoO}_{3-\delta}$ (GBCO)	$\text{Gd}_{0.5}\text{Ba}_{0.5}\text{CoO}_{2.625}$	0.35 ($T=973$ K, $P(\text{O}_2)=0.2$ atm) ⁴³
$\text{La}_{0.6}\text{Sr}_{0.4}\text{Co}_{0.2}\text{Fe}_{0.8}\text{O}_{3-\delta}$ (LSCF)	$\text{La}_{0.625}\text{Sr}_{0.375}\text{Co}_{0.25}\text{Fe}_{0.75}\text{O}_3$	<0.03 ($T=973$ K, $P(\text{O}_2)=0.2$ atm) ⁴⁵
$\text{La}_{0.8}\text{Sr}_{0.2}\text{CoO}_{3-\delta}$ (LSC)	$\text{La}_{0.75}\text{Sr}_{0.25}\text{CoO}_3$	<0.01 ($T=973$ K, $P(\text{O}_2)=0.2$ atm) ⁴¹
$\text{LaCoO}_{3-\delta}$ (LCO)	LaCoO_3	< 0.01 ($T=973$ K, $P(\text{O}_2)=0.1$ atm) ⁴¹
$\text{La}_{0.8}\text{Sr}_{0.2}\text{MnO}_{3-\delta}$ (LSM)	$\text{La}_{0.75}\text{Sr}_{0.25}\text{MnO}_3$	-0.03 ($T=973$ K, $P(\text{O}_2)=0.2$ atm) ⁴⁶
$\text{LaMnO}_{3-\delta}$ (LMO)	$\text{La}_{0.9375}\text{Mn}_{0.9375}\text{O}_3$ ($\text{LaMnO}_{3.2}$)	-0.15 (due to cation vacancies) ($T=973$ K, $P(\text{O}_2)=0.2$ atm) ⁴⁶

Figures S3 and S4 show the experimentally measured ASR and k^* , respectively, plotted against the calculated bulk O p -band center values for the off-stoichiometric structures given in Table S3. It can be seen that not only do the correlations identified in the stoichiometric data (Figures 1 and 2 in the main text) persist, but the linear correlations are actually more accurate. Furthermore, the separation of the LSM family Figure S3, due to its different ORR mechanism, is even more pronounced than in Figure 1 of the main text. It is reasonable to expect that, if a descriptor is truly capturing the essential physics in a process, then the accuracy of the descriptor will be improved when the descriptor value is determined from systems which more accurately reflect those used in obtaining the experimental data. Such an effect is exactly what is seen here, where an improved correlation between the experimental data and our descriptor is observed when more accurate structures are used. Therefore, this result further supports that the O p -band descriptor is capturing essential physics of the system. These results also suggest that, when possible, use of the correct stoichiometry is preferable. However, obtaining the stoichiometry from experiment requires the system to be made and characterized, and therefore may not be practical when exploring many new materials.

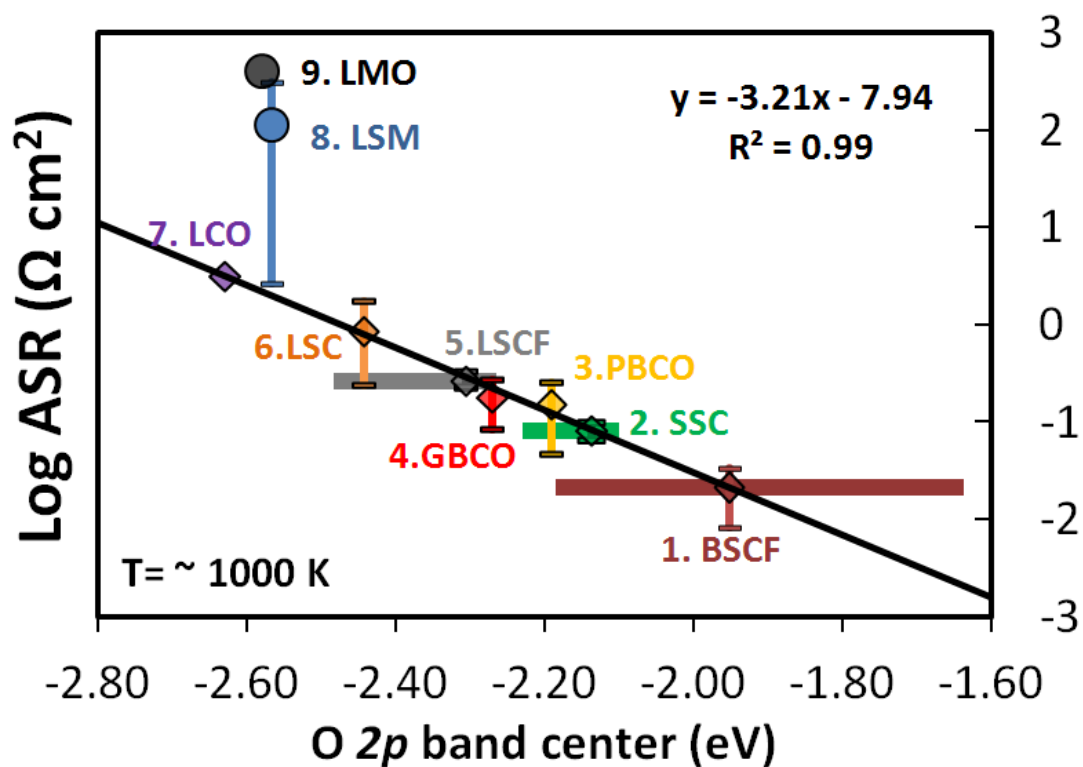


Figure S3: Experimental area specific resistances at ~ 1000 K (experimental data the same as in Figure 1 of the main paper) vs. the calculated bulk O p -band center. The systems and compositions used in the calculations are given in Table S2. Concentrated disordered systems yield a range of calculated O p -band center values that are represented with horizontal lines. The method of treating these systems is given in Section S2.

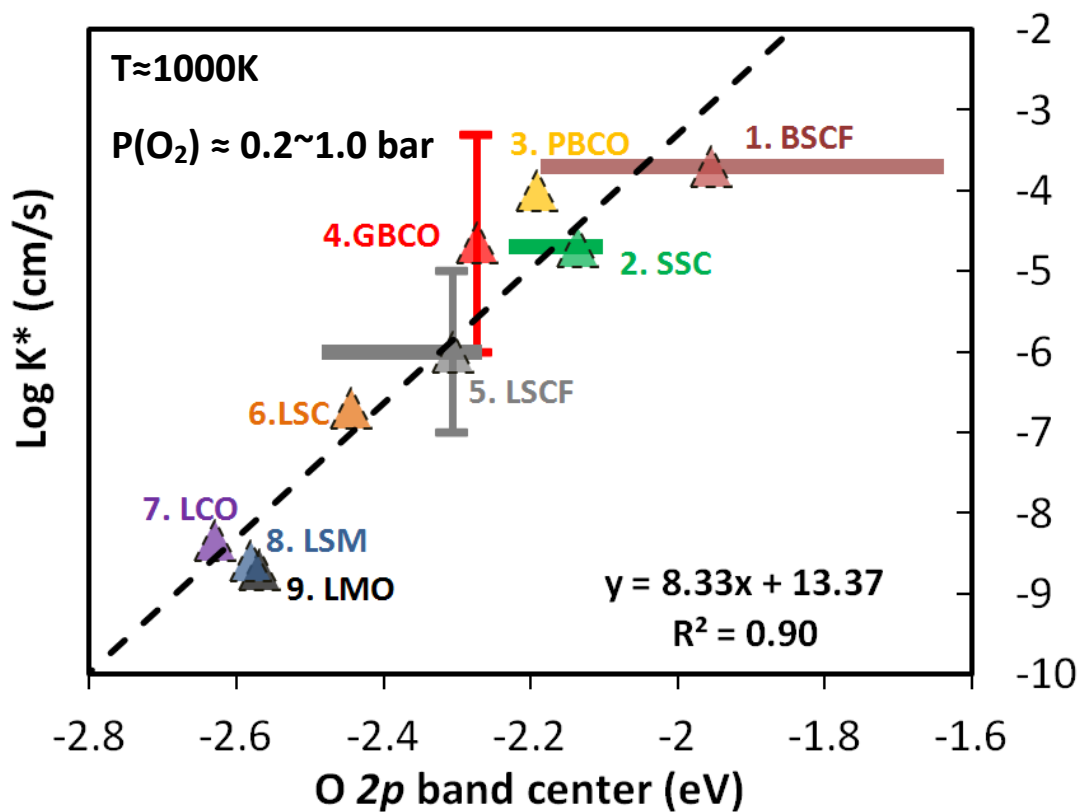


Figure S4: Experimental surface exchange coefficients k^* (experimental data the same as in Figure 2 of the main paper) vs. the calculated bulk O *p*-band center. The systems and compositions used in the calculations are given in Table S2. Concentrated disordered systems yield a range of calculated O *p*-band center values which are represented with horizontal lines. The method of treating these systems is given in Section S2.

Section 7: The Bulk Vacancy Formation Energy as an Alternative Descriptor

The O *p*-band correlates with many other first-principles and experimental properties. Since correlation is approximately transitive (if A correlates with B, and B correlates with C, then A correlates with C), then any parameter that correlates with the O *p*-band could be used as a descriptor in its place. That said, the correlation between key properties (e.g., ASR and k^*) and some parameters might be worse (or potentially better) than with O *p*-band center. Some parameters may be advantageous to consider in place of O *p*-band center as a descriptor, either because they are easier to determine from calculation or experiment or because they are more intuitive to think about. Here we explicitly consider the bulk oxygen vacancy formation energies (E_{bulk_vac}) as a descriptor as it is often known from experiment and widely considered in intuitive and quantitative models of the ORR.

Figures S5 and S6 show the experimentally measured ASR and k^* , respectively, plotted against the calculated bulk oxygen vacancy formation energy (E_{bulk_vac}). E_{bulk_vac} is determined by finding the most stable vacancy site of the most stable nonstoichiometric perovskites among the sampled structures (see Table S3 for stoichiometries used). For the perovskites with dilute defects/doping (LSM, LMO, LCO, and LSC) and for the ordered phase with a specified configuration (PBCO and GBCO), we explored all the symmetry distinct oxygen sites in the simulated supercell to determine the most stable E_{bulk_vac} . For disordered perovskites with high defect/doping concentration such as LSCF, SSC, and BSCF, we took the most stable SQS structure among our sampled 2×2×2 perovskite supercell configurations and determined the most stable E_{bulk_vac} within this one SQS

structure. The experimental ASRs and k^* s are the same as in Figure 1 and Figure 2 of the main paper. The E_{bulk_vac} are calculated from the relation:

$$E_{bulk_vac} = \left[E_{defected_bulk} - E_{bulk} + \frac{1}{2}(E_{O_2} + \Delta h^{O_2}_{correction}) \right] \dots\dots (1)$$

Where E_{bulk} , $E_{defected_bulk}$, E_{O_2} , and $\Delta h^{O_2}_{correction}$ are the calculated total energies of a perovskite bulk with the simulated composition shown in Table S3, the simulated off-stoichiometric perovskite bulk with an oxygen vacancy (at the most stable vacancy site), an O_2 molecule, and the energy correction of O_2 (0.33 eV/ O_2 for PW91 soft oxygen pseudopotential as reported in Ref. ³³) respectively. For compounds represented with SQS's (see Section 2) the most stable SQS explored was used to determine the vacancy formation energy. Notice that the calculation of $E_{defected_bulk}$ needs to explore different defect-dopant configurations to find the most stable site for oxygen vacancy formation. Different defect-dopant configurations can have E_{bulk_vac} vary by 1~2 eV. For example, our calculations show that the ordered double perovskite $PrBaCo_2O_{5+\delta}$ has the E_{bulk_vac} of oxygen in the Pr plane ~1.5 eV more stable than that of the Ba plane. As more catalytically active perovskite oxides (e.g. $Ba_{0.5}Sr_{0.5}Co_{0.8}Fe_{0.2}O_{3-\delta}$, $Sm_{0.5}Sr_{0.5}CoO_{3-\delta}$, etc) tend to have higher dopant and oxygen vacancy concentration, the determination of E_{bulk_vac} will generally be much more computational demanding than using the bulk O p -band center as the ORR descriptor. Figures S5 and S6 show correlations similar in quality to those seen in Figures 1 and 2 of the main text with the O p -band center descriptor. These results demonstrate that E_{bulk_vac} is also a good descriptor for the ORR in these SOFC cathode systems.

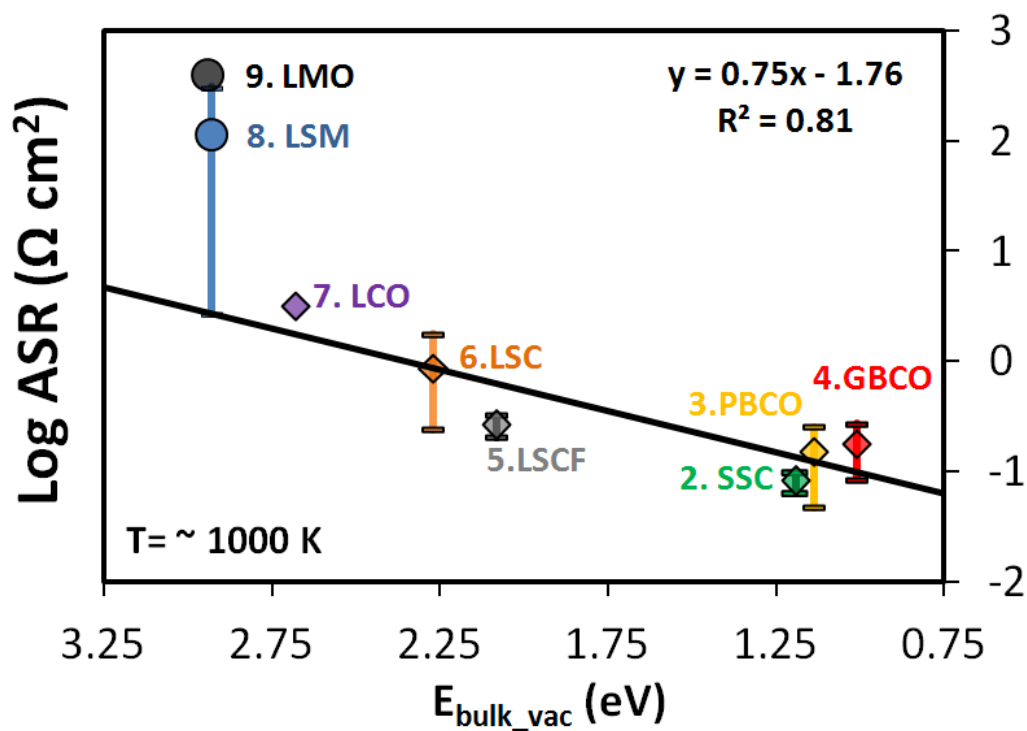


Figure S5: The experimental ASR (experimental data the same as in Figure 1 of the main paper) as a function of the E_{bulk_vac} . The systems and compositions used in the calculations are given in Table S3. E_{bulk_vac} s are calculated based on the most stable oxygen site in the simulated bulk according to the method described in Section S6.

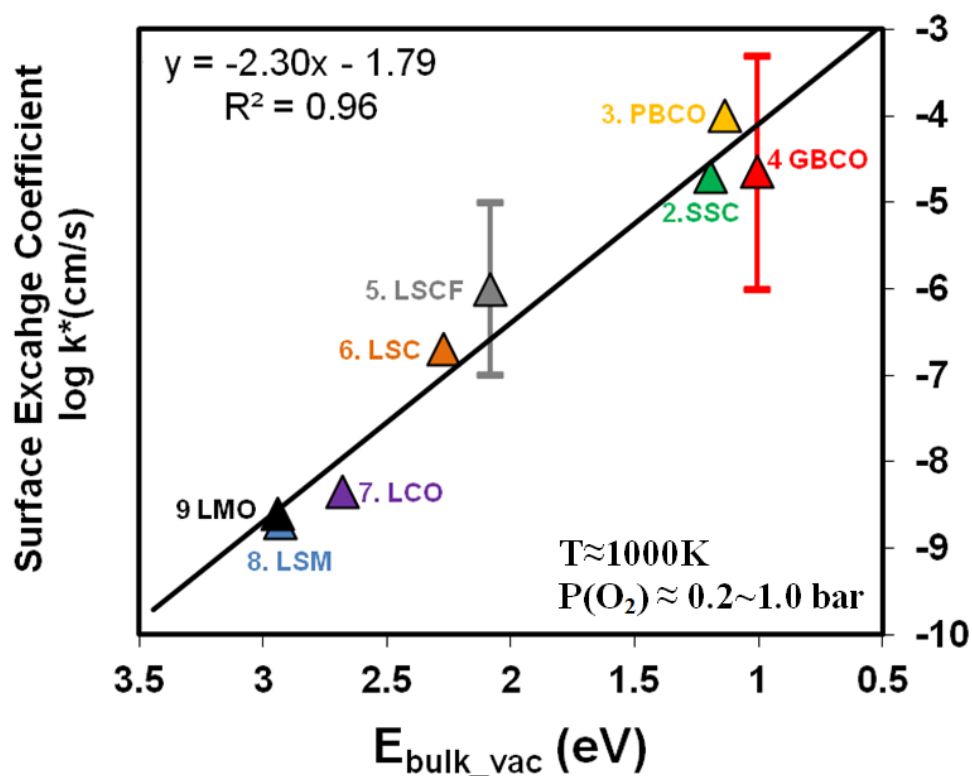


Figure S6: The experimental surface exchange coefficient k^* (experimental data the same as in Figure 2 of the main paper) as a function of the $E_{\text{bulk_vac}}$. The systems and compositions used in the calculations are given in Table S3. $E_{\text{bulk_vac}}$ s are calculated based on the most stable oxygen site in the simulated bulk according to the method described in Section S6.

Section 8: Material Stability

Figure S7 shows the ORR activity (assumed to be equal to $1/ASR$) as a function of the O p -band center, which suggests that all the perovskite systems typically considered for SOFC cathodes reside on the upward sloping side of the expected volcano plot and that weaker oxygen binding (higher O p -band values) may yield improved SOFC catalytic materials. However, as the binding of the materials becomes weaker, they also become less stable, which limits their practical use as SOFC cathodes. For example, the predicted ORR activity of $LaNiO_3$ based on the calculated bulk O p -band center (represented with an empty circle in Figure S7) is close to that of BSCF, but in practice $LaNiO_3$ is not stable under SOFC conditions as it decomposes to the Ruddlesden-Popper phase $La_{n+1}Ni_nO_{3n+1}$ and NiO⁴⁷⁻⁴⁸. This stability trend suggests that the optimization of SOFC catalysts with the O p -band descriptor needs to take into account the oxide stability at SOFC conditions. Stability screening can be performed by including an additional material stability descriptor to search for the best possible compromise between activity and stability, perhaps using the Pareto-optimal plot as suggested in Ref. ⁴⁹. As stability is likely correlated with the ability to form vacancies, which in turn correlates with the O p -band center, the O p -band center may also provide a good descriptor for stability. However, additional work is needed in this area to assess a robust descriptor for stability.

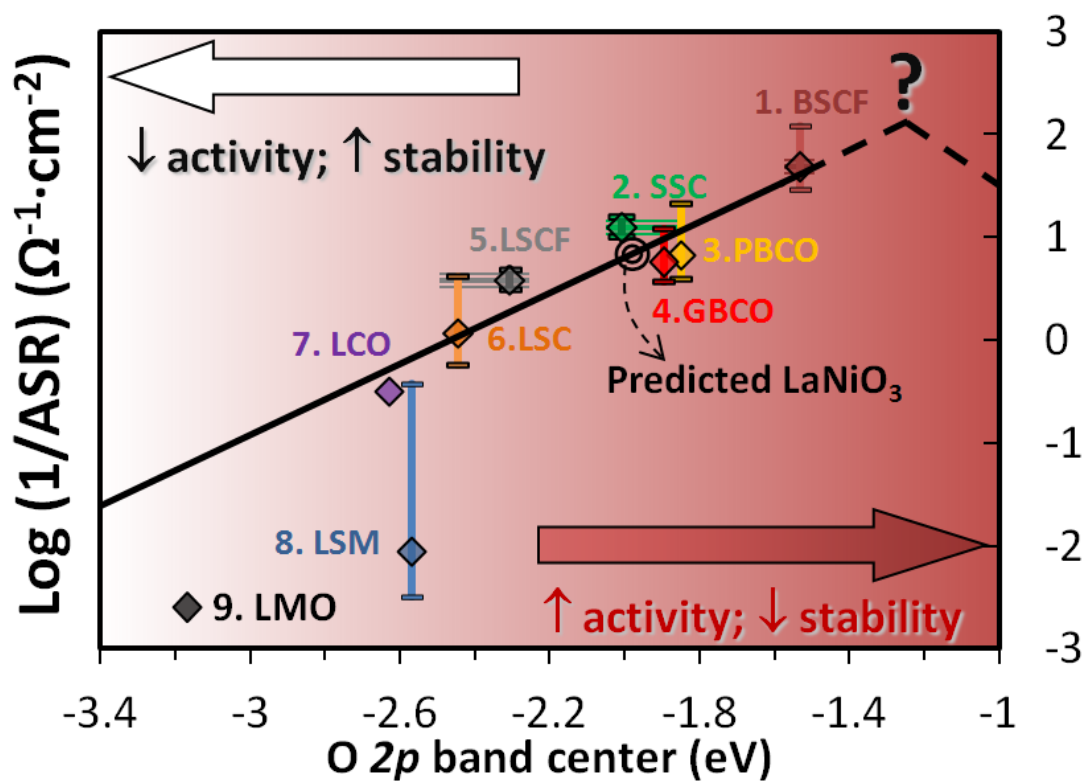


Figure S7: The ORR activity (represented as $1/\text{ASR}$) at $T \approx 1000\text{K}$ and $P(\text{O}_2) \approx 0.2$ bar as a function of the O p -band center. Experimental data labeled 1-9 are the same as in Figure 1 of the main paper and the empty circle represents the predicted ORR activity of LaNiO_3 . The extended dashed line is hypothesized based on the volcano plot typically seen for catalyst activity as a function of a descriptor correlated with binding energies. The shaded area suggests the region where material stability is potentially too low for SOFC applications.

References

1. Z. P. Shao and S. M. Haile, *Nature*, 2004, **431**, 170-173.
2. S. Lee, Y. Lim, E. A. Lee, H. J. Hwang and J.-W. Moon, *J. Power Sources*, 2006, **157**, 848-854.
3. C.-H. Chen, C.-L. Chang and B.-H. Hwang, *Materials Chemistry and Physics*, 2009, **115**, 478-482.
4. C. Xia, W. Rauch, F. Chen and M. Liu, *Solid State Ionics*, 2002, **149**, 11-19.
5. H. Lv, Y. J. Wu, B. Huang, B. Y. Zhao and K. A. Hu, *Solid State Ionics*, 2006, **177**, 901-906.
6. S. W. Baek, J. H. Kim and J. Bae, *Solid State Ionics*, 2008, **179**, 1570-1574.
7. G. Kim, S. Wang, A. J. Jacobson, L. Reimus, P. Brodersen and C. A. Mims, *J. Mater. Chem.*, 2007, **17**, 2500-2505.
8. C. Zhu, X. Liu, C. Yi, D. Yan and W. Su, *J. Power Sources*, 2008, **185**, 193-196.
9. D. Chen, R. Ran, K. Zhang, J. Wang and Z. Shao, *J. Power Sources*, 2009, **188**, 96-105.
10. A. Chang, S. J. Skinner and J. A. Kilner, *Solid State Ionics*, 2006, **177**, 2009-2011.
11. A. Tarancon, S. J. Skinner, R. J. Chater, F. Hernandez-Ramirez and J. A. Kilner, *J. Mater. Chem.*, 2007, **17**, 3175-3181.
12. N. Li, Z. Lü, B. Wei, X. Huang, K. Chen, Y. Zhang and W. Su, *Journal of Alloys and Compounds*, 2008, **454**, 274-279.
13. S. P. Jiang, *Solid State Ionics*, 2002, **146**, 1-22.

14. J. M. Ralph, C. Rossignol and R. Kumar, *Journal of the Electrochemical Society*, 2003, **150**, A1518-A1522.
15. A. Esquirol, N. P. Brandon, J. A. Kilner and M. Mogensen, *Journal of the Electrochemical Society*, 2004, **151**, A1847-A1855.
16. T. Horita, K. Yamaji, N. Sakai, H. Yokokawa, A. Weber and E. Ivers-Tiffée, *Journal of the Electrochemical Society*, 2001, **148**, A456-A462.
17. M. Shiono, K. Kobayashi, T. Lan Nguyen, K. Hosoda, T. Kato, K. Ota and M. Dokiya, *Solid State Ionics*, 2004, **170**, 1-7.
18. Y. Takeda, R. Kanno, M. Noda, Y. Tomida and O. Yamamoto, *Journal of the Electrochemical Society*, 1987, **134**, 2656-2661.
19. E. Perry Murray and S. A. Barnett, *Solid State Ionics*, 2001, **143**, 265-273.
20. T. Ioroi, T. Hara, Y. Uchimoto, Z. Ogumi and Z. Takehara, *Journal of the Electrochemical Society*, 1998, **145**, 1999-2004.
21. L. Wang, R. Merkle, J. Maier, T. Acarturk and U. Starke, *Applied Physics Letters*, 2009, **94**, 071908.
22. I. C. Fullarton, J. P. Jacobs, H. E. van Benthem, J. A. Kilner, H. H. Brongersma, P. J. Scanlon and B. C. H. Steele, *Ionics*, 1995, **1**, 51.
23. A. A. Taskin, A. N. Lavrov and Y. Ando, *Applied Physics Letters*, 2005, **86**.
24. J. E. tenElshof, M. H. R. Lankhorst and H. J. M. Bouwmeester, *Solid State Ionics*, 1997, **99**, 15-22.
25. J. A. Lane, S. J. Benson, D. Waller and J. A. Kilner, *Solid State Ionics*, 1999, **121**, 201-208.
26. R. A. De Souza and J. A. Kilner, *Solid State Ionics*, 1999, **126**, 153-161.

27. T. Ishigaki, S. Yamauchi, J. Mizusaki, K. Fueki and H. Tamura, *Journal of Solid State Chemistry*, 1984, **54**, 100-107.
28. A. V. Berenov, J. L. MacManus-Driscoll and J. A. Kilner, *Solid State Ionics*, 1999, **122**, 41-49.
29. S. H. Wei, L. G. Ferreira, J. E. Bernard and A. Zunger, *Physical Review B*, 1990, **42**, 9622.
30. T. Arima, Y. Tokura and J. B. Torrance, *Physical Review B*, 1993, **48**, 17006-17009.
31. K. Tobe, T. Kimura, Y. Okimoto and Y. Tokura, *Physical Review B*, 2001, **64**, 184421.
32. N. N. Kovaleva, A. V. Boris, C. Bernhard, A. Kulakov, A. Pimenov, A. M. Balbashov, G. Khaliullin and B. Keimer, *Physical Review Letters*, 2004, **93**, 147204
33. Y.-L. Lee, J. Kleis, J. Rossmeisl and D. Morgan, *Physical Review B (Condensed Matter and Materials Physics)*, 2009, **80**, 224101.
34. J. A. Kilner, R. A. De Souza and I. C. Fullarton, *Solid State Ionics*, 1996, **86-88**, 703-709.
35. R. Merkle, J. Maier and H. J. M. Bouwmeester, *Angewandte Chemie-International Edition*, 2004, **43**, 5069-5073.
36. J. Maier, *Solid State Ionics*, 2000, **135**, 575-588.
37. L. Wang, T. Maxisch and G. Ceder, *Physical Review B*, 2006, **73**, 195107.
38. H. Wang, Y. Cong and W. Yang, *Journal of Membrane Science*, 2002, **210**, 259-271.

39. S. McIntosh, J. F. Vente, W. G. Haije, D. H. A. Blank and H. J. M. Bouwmeester, *Solid State Ionics*, 2006, **177**, 1737-1742.
40. E. Bucher, A. Egger, P. Ried, W. Sitte and P. Holtappels, *Solid State Ionics*, 2008, **179**, 1032-1035.
41. J. Mizusaki, Y. Mima, S. Yamauchi, K. Fueki and H. Tagawa, *Journal of Solid State Chemistry*, 1989, **80**, 102-111.
42. C. Frontera, A. Caneiro, A. E. Carrillo, J. Oro-Sole and J. L. Garcia-Munoz, *Chemistry of Materials*, 2005, **17**, 5439-5445.
43. A. A. Taskin, A. N. Lavrov and Y. Ando, *Physical Review B*, 2005, **71**.
44. J. Mizusaki, M. Yoshihiro, S. Yamauchi and K. Fueki, *Journal of Solid State Chemistry*, 1985, **58**, 257-266.
45. D. Mantzavinos, A. Hartley, I. S. Metcalfe and M. Sahibzada, *Solid State Ionics*, 2000, **134**, 103-109.
46. J. Mizusaki, N. Mori, H. Takai, Y. Yonemura, H. Minamiue, H. Tagawa, M. Dokiya, H. Inaba, K. Naraya, T. Sasamoto and T. Hashimoto, *Solid State Ionics*, 2000, **129**, 163-177.
47. H. E. Hofer and W. F. Kock, *Journal of the Electrochemical Society*, 1993, **140**, 2889-2894.
48. M. Zinkevich and F. Aldinger, *Journal of Alloys and Compounds*, 2004, **375**, 147-161.
49. J. Greeley and M. Mavrikakis, *Nat. Mater.*, 2004, **3**, 810-815.